IOP Publishing Nanotechnology
Nanotechnology 32 (2021) 185203 (9pp) https://doi.org/10.1088/1361-6528/abe003

Crystallinity-dependent device characteristics of polycrystalline 2D $n = 4$ Ruddlesden–Popper perovskite photodetectors

Junwoo Kim, Woocheol Lee, Kyungjune Cho[1], Heebeom Ahn, Jonghoon Lee, Kyeong-Yoon Baek, Jae-Keun Kim, Keehoon Kang* and Takhee Lee*

Department of Physics and Astronomy, and Institute of Applied Physics, Seoul National University, Seoul 08826, Republic of Korea

E-mail: keehoon.kang@snu.ac.kr and tlee@snu.ac.kr

Received 3 October 2020, revised 27 December 2020
Accepted for publication 26 January 2021
Published 12 February 2021

Abstract

Ruddlesden–Popper (RP) perovskites have attracted a lot of attention as the active layer for optoelectronic devices due to their excellent photophysical properties and environmental stability. Especially, local structural properties of RP perovskites have shown to play important roles in determining the performance of optoelectronic devices. Here, we report the photodetector performance variation depending on the crystallinity of $n = 4$ two-dimensional (2D) RP perovskite polycrystalline films. Through controlling the solvent evaporation rate, 2D RP perovskite films could be tuned between highly- and randomly-orientated phases. We investigated how different factors related to the film crystallinity are reflected in the variation of photodetector performances by considering grain boundary and low energy edge state effects in $n = 4$ RP perovskites. Better understanding the interplay between these factors that govern the photophysical properties of the devices would be beneficial for designing high-performance RP perovskite-based optoelectronic devices.

Supplementary material for this article is available online

Keywords: perovskites, crystallinity, photodetectors, grain boundary, optoelectronic devices

(Some figures may appear in colour only in the online journal)

1. Introduction

Organo-halide perovskites (OHP) have being widely studied for their excellent photophysical properties such as high absorption coefficient, low exciton binding energy, long carrier diffusion length, and relatively high carrier mobility. These characteristics have motivated various researches for many fields including photovoltaics [1–5], light-emitting diodes (LEDs) [6–11], memories [12, 13], transistors [14–16], and photodetectors [17]. However, it is also known that OHPs have poor environmental stability, especially against moisture [18–20]. In addition, the ion migration in perovskites hinders exhibiting consistent performance and suffers from degradation of perovskites [21, 22]. In order to overcome these issues, two-dimensional (2D) perovskites have been developed which have organic spacers that keep water from penetrating to the inorganic part of OHP [23, 24]. Up to now, several kinds of 2D perovskites have been developed; Ruddlesden–Popper

[1] Present address: Max Planck Institute of Microstructure Physics, Halle 06120, Germany.
* Authors to whom correspondence should be addressed.

(RP) perovskites [25, 26], Dion–Jacobson perovskites [27], and perovskites with alternating cations in the interlayer space [28]. Among them, RP perovskites with the chemical formula, $B_2A_{n-1}M_nX_{3n-1}$, where B is an organic spacer ion (e.g. butylammonium), A is a small cation (methylammonium), M is a metal ion (e.g. Pb^{2+} or Sn^{2+}) and X is halide (e.g. Cl^-, Br^- or I^-), have been actively studied for optoelectronic applications due to their common structures [29–32]. For high device performance, it is desired to use single crystalline RP perovskites but they are difficult to controllably synthesize large-area films for device fabrication. Therefore, for practical applications, researches on polycrystalline films are as essential for the application of large-area solution-processible devices.

When using polycrystalline materials for an optoelectronic device, crystal domain size evidently plays a crucial role in the device performance. In general, a large crystal size has been correlated to good device performances due to a better charge transport within the large crystals. However, specifically for 2D RP perovskites, it is essential to also consider the relative orientations of the crystal domains because of the presence of insulating organic spacers through which the charge transport is expected to be hindered. From several preceding studies, different lattice orientations of RP perovskites films have been engineered via various solvent-engineering methods for different types and structures of optoelectronic devices [33–35]. In case of vertical device structures (e.g. solar cells and LEDs), it is beneficial to have vertically orientated structure of RP perovskites [33]. In contrast, for lateral-structure devices (e.g. photodetectors), lateral orientation may be preferred to aid charge transport of photo-generated carriers between the electrodes [34]. Representatively, Wang *et al* demonstrated that the performance of RP perovskite single crystal photodetector surpasses in the laterally-oriented device compared to the vertically-oriented one [35]. As such, both the crystal domain size and the crystal orientation become important factors that should be considered for polycrystalline thin-film RP perovskite devices.

Here, we fabricated solution-processed 2D RP lead iodide $n = 4$ perovskite ($BA_2MA_3Pb_4I_{13}$, where BA is butylammonium and MA is methylammonium cations) polycrystalline photodetectors to compare the device performances between highly-orientated (HO) and randomly-orientated (RO) RP perovskites. Referring to the previous studies, we successfully controlled the crystal size and relative crystal orientations of RP perovskite films through controlling the solvent evaporation rate. Through this, we compared the photodetector performance variation of polycrystalline RP perovskites for both HO and RO films. Additionally, we investigated the temperature-dependent device characteristics in both types of devices to compare the degree of ion migration and the effect of shallow traps. These results will give better insight to understanding polycrystalline thin-film optoelectronic device applications of RP perovskites.

2. Experimental details

2.1. Synthesis of RP Perovskites

PbO powders, hydrophosphorous acid (H_3PO_2, 50 wt% in H_2O), and hydroiodic acid (HI, 57 wt% in H_2O) are purchased from Sigma-Aldrich. Methylammonium iodide (MAI) and n-butylammonium iodide (BAI) are obtained from Greatcell Solar Materials Ltd. In this study, $n = 4$ RP perovskites were selected due to their excellent optical properties, such as a low exciton binding energy and high photocurrent among $n = 1-5$ RP perovskites series [35–37]. To make $n = 4$ RP perovskite single crystals, 2.665 g of PbO powders, 1.423 g of MAI, and 0.6 g of BAI are dissolved into a mixture containing 15 ml of HI and 2 ml of H_3PO_2. With stirring, the mixed solution was heated to 120 °C on a hot plate until whole ingredients were perfectly dissolved. After that, the solution is cooled at room temperature, and $n = 4$ RP perovskite single crystals are formed. The powder XRD data (see figure S1 (available online at stacks.iop.org/NANO/32/185203/mmedia)) was well-matched with previous results with $n = 4$ RP perovskite single crystals [35, 36]. Then, the crystal pieces are collected after pouring the solution through a Whatman filter paper. The final crystals are dried in a vacuum chamber over 6 h. For spin-coating, we used the single crystal-dissolved solution rather than the solution mixed with precursors, to optimize stoichiometric ratio for the $n = 4$ film formation with high purity. From the x-ray photoelectron spectroscopy data (figure S2), we calculated the relative atomic concentrations ratio of Pb and I of both HO and RO films (ideally 1:3.25), which are 1:3.17 for the HO phase and 1:3.26 for the RO phase. Two types of solutions are prepared; gamma-butyrolactone (GBL)-based solution of a concentration of 1 M and dimethylformamide (DMF)-based solution of a concentration of 0.5 M. If the concentrations of the two solutions are set as above, the thickness of those films after spin-coating become almost the same (≈160 nm), so that the thickness variable in the device performance can be neglected.

2.2. Photodetector device fabrication

First, 270 nm SiO_2/heavily doped p++ Si substrates are cleaned using acetone, isopropyl alcohol (IPA), and DI water in a sonicator and dried through a N_2 blowgun. Then, the substrates are treated with a reactive ion etcher using O_2 plasma (30 sccm, 50 W) for 120 s to remove residual organic leftover and make the substrates more hydrophilic. 30 μl solutions prepared above are spin-coated on the substrates at 3000 rpm for 30 s in a N_2-filled glove box in the condition less than 0.5 ppm for H_2O and 2 ppm for O_2. In case of the 1 M GBL solution, spin-coating process is performed without stopping, whereas 10 μl of toluene is dripped during spin-coating for the 0.5 M DMF solution. After the spin-coating, Au (50 nm)/Ti (5 nm) layers are deposited on the coated film at a rate of 0.5 Å s^{-1} using an electron-beam evaporator. The electrodes are patterned with a shadow mask which has 50 μm for channel length and 1 mm for channel width.

Prepared samples are transferred to a probe station vacuum chamber to perform photoelectric measurement.

2.3. Film and device characterization

All optoelectronic measurements including temperature-dependent experiments were performed by a semiconductor parameter analyser (Keithley 4200 SCS) in vacuum ($\sim 10^{-6}$ Torr). The temperature of the device was adjusted by injecting liquid N_2 to the vacuum chamber with a temperature controller. The light source was a 520 nm dot laser (Su Semiconductor). High resolution x-ray diffraction (XRD) spectra and pole figures were collected by Rigaku SmartLab under the condition of 45 kV and 200 mA. The photoluminescence data was collected by XperRAM 200 (Nanobase Inc.) by using 532 nm laser source with spot size of ~ 1 μm. Time-resolved photoluminescence (TRPL) mapping was conducted by XperRF (Nanobase Inc.) using 454 nm pulse laser with the intensity of 200 nW and the rate of 2500 kHz, in the ambient condition. The atomic force microscope (AFM) images were obtained with a non-contact mode by NX-10 (Park Systems). The field-emission scanning electron microscope (FE-SEM) images were collected using JSM-6700F (JEOL Ltd). The absorbance spectra were obtained by V-770 (Jasco).

3. Results and discussion

We controlled the crystallinity of $n = 4$ RP perovskite films via solvent-engineering process. It has been previously reported that crystallinity can be tuned by controlling the solvent evaporation rate [38, 39]. In particular, Chen *et al* systematically found that a slow solvent removal (e.g. using gamma-butyrolactone) causes low supersaturation of perovskite solution, which results in a HO vertical phase with the high degree of the crystallinity whereas a fast solvent removal (e.g. anti-solvent dropping) induces many nucleation sites, which leads to a RO phase with the low degree of the crystallinity [39]. Based on these results, we chose GBL as the solvent for fabricating HO films and DMF solvent with toluene dropping for RO films for slow and fast solvent removal, respectively. As a result of the aforementioned spin-coating methods, we could successfully distinguish between HO and RO structures of $n = 4$ RP perovskites polycrystalline films. The schematic images of these two phases are shown in figure 1(a). In the HO phase (left image of figure 1(a)), the crystal growth starts from the liquid–air surface, and as the GBL slowly evaporates, the nucleation due to supersaturation inside the solution does not occur, resulting in the top-crust to grow consistently all the way down to the substrate. In contrast, a fast solvent evaporation using anti-solvents (toluene, in this work) causes supersaturation inside the solution, creating many nucleation sites. Accordingly, the crystal growth occurs in various places, and therefore the entire film has no preferred lattice orientations (right image of figure 1(a)). We demonstrated the crystallographic orientation information of each film using XRD and pole figure analysis. The corresponding XRD data are shown in figure 1(b). From previous theoretical and experimental data, it is known that the diffraction peaks of crystalline $n = 4$ RP perovskites locate around 14.1° and 28.3° which correspond to the crystallographic planes (111) and (202), respectively [35]. Although some phases other than $n = 4$ seem to be present from our UV–vis data (figure S3), an excellent agreement between our XRD data of the HO phase and the diffraction peak positions stated above suggest that $n = 4$ is the dominant phase in the film. In the anti-solvent dropping case, there appears to be no preferred orientations from the XRD data with several broad peaks distributed in a wide range, indicating the RO phase, which resembles previous results by Chen *et al* where they observed diffuse XRD ring for $n = 4$ 2D perovskite films with a low degree of vertical orientation [38, 39]. When using only DMF, which has a moderate evaporation rate relative to GBL and DMF with anti-solvent engineering, we could not obtain clear preferential orientations with broader peaks and weaker intensities compared to the GBL case (see figure S4 in the supplementary data). In all the films, no significant amount of extrinsic defects such as PbI_2 were detected as seen from the lack of diffraction peaks at $2\theta = 12.6°$ and 26.3°. From the pole figures we obtained, it was observed that the HO phase had preferred orientations towards (111) (figure S5(a)) and (202) (figure S5(c)) via high diffraction intensities at the center of each stereographic plane. Such sharp diffraction spots lack in the RO phase and a broad diffraction ring appears in the (111) pole figure data of the RO phase (figure S5(b)), which indicates random in-plane orientation and relatively disordered vertical orientation of the RO phase film. The randomly orientated nature is further supported by a flat intensity distribution shown from (202) pole figure data (figure S5(d)).

The schematic image of the fabricated photodetector and $n = 4$ RP perovskite crystal structure are illustrated in figure 1(c). Film morphologies measured by AFM and cross-sectional images obtained by FE-SEM are shown in figure 1(d). As shown in this figure, the grain sizes of the HO perovskite film distributed from hundreds of nm to 1 μm (310 nm on average), which are much larger than those of the RO film. In the RO phase, by the rapid crystallization process with creation of many nucleation sites via anti-solvent dropping, the grain size inevitably becomes small (67 nm on average), and the opposite phenomenon occurs in the HO phase. Distribution of grain sizes is shown in supplementary data (figure S7). We will show how these factors would contribute to the different device characteristics of the photodetectors.

Figure 2 shows device performances of the photodetectors made with HO and RO phase. In figure 2(a), voltage–current (V_d–I_d) curves under dark and light condition are shown. The dark currents of the two devices appeared relatively similar, less than an order of magnitude difference. But under the light condition, the photocurrent of the photodetector device made of HO phase film ('HO device') was larger than that of the device made of RO phase film ('RO device') by more than an order of magnitude. The optical switching characteristics under the bias of 10 V are shown in figure 2(b). The rise and decay times were both less than

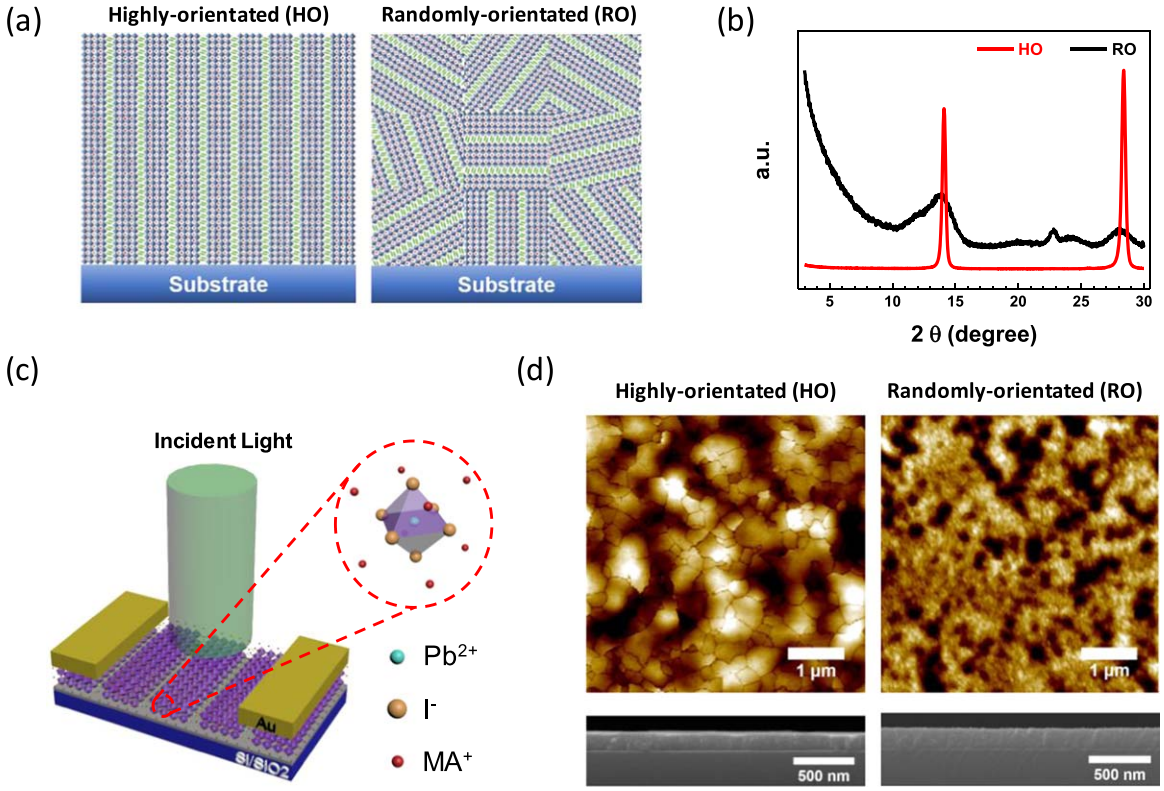

Figure 1. (a) Schematic illustration of the spin-coated $n = 4$ RP perovskite films with the HO and RO phases. (b) XRD data of the HO and RO films. (c) Schematic image of the $n = 4$ RP perovskite photodetector. (d) AFM and cross-sectional FE-SEM images of the HO and RO phase films.

30 ms, which is the limit of our measurement equipment. The On/Off ratios were over 10^2 for the RO phase and 10^3 for the HO phase. Figures 2(c) and (d) show responsivity and detectivity of these two types of perovskites photodetectors. In photodetector devices, responsivity (R) represents a quantitative measure of how much excess electrical current output comes out when illuminated with light input, and specific detectivity (D^*) indicates the magnitude of the signal to noise ratio of a photodetector per unit bandwidth and unit area. In details, the responsivity of a photodetector is given by $R = (I_{\text{light}} - I_{\text{dark}})/(PA)$, where I_{light} is the current under illumination, I_{dark} is the dark current, P is the light intensity (12.7 mW cm^{-2}), and A is the device area (width of 1 mm and channel length of 50 μm). The detectivity of a photodetector is represented by $D^* = RA^{0.5}/(2eI_{\text{dark}})^{0.5}$, where R is the responsivity, A is the device area, and e is the electric charge [40]. In the HO phase, the R and D^* values measured at 10 V were found to be approximately 5.3 mA W^{-1} and 4.6×10^9 Jones, respectively, which were about an order of magnitude larger than those of the RO phase. Our performance values are somewhat lower than the results reported in previous studies for devices made with single crystals [35, 41] but comparable with that of a thin-film [30].

This variation in the photodetector performance between the two kinds of devices can be ascribed to several inter- and intra-crystal domain factors: different density of grain boundaries (GBs) and the relative alignment directions of the inorganic perovskite parts, and insulating organic spacer parts within the RP crystals [34, 35]. The schematic images that represent the morphology of each film are shown in figures 3(a) and (b). Generally, a larger grain size is preferred for the charge transport in optoelectronic devices, due to a lower density of GBs which can act as trap sites [42]. We have directly tested the grain size-dependence of photodetector device performance in the HO devices (see figure S8 in supplementary data). The larger the grain size, the larger the dark and photocurrent values, which supports the better charge transport in the larger-grain devices. This results in a higher responsivity and detectivity values of the devices. In light of this result, as shown from our film characterizations (see figure 1), it is natural to expect that the photodetector performance of the HO phase is significantly better than that of the RO phase. This also accounts for the larger dark and photo-current of the HO device than RO device. However, one should be cautious of neglecting the relative crystal orientations between the grains, owing to the presence of insulating organic spacers. Unlike the GB effect, the orientation effect can slightly favor charge transport in RO device since the random orientation of the crystals can improve connection between the inorganic perovskite parts [43]. However, in our devices the density of traps in GBs appears to be a dominant factor in determining the device performance, according to our device performance data.

We also investigated the photophysical properties of the HO and RO films to understand the large difference in the device performance between the two kinds of devices. The photodetector relies on conversion of photo-generated

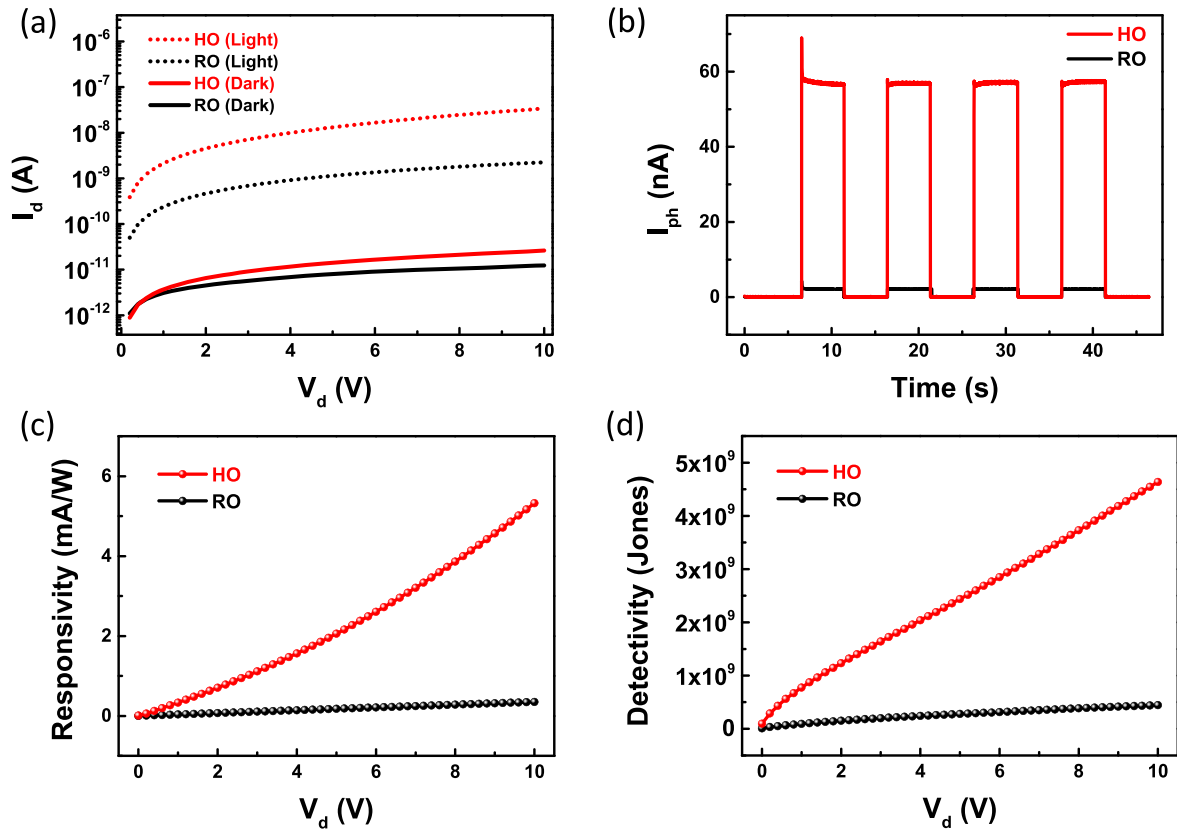

Figure 2. (a) $I-V$ curves of the HO and RO photodetector devices. (b) Optical switch characteristics of the HO and RO devices under a 520 nm light irradiation. (c) Responsivity versus voltage behavior under the irradiance at 520 nm for the both HO and RO devices. (d) Specific Detectivity versus voltage behavior under the irradiance at 520 nm for the both HO and RO devices.

excitons into free electrons and holes that can be harnessed into currents (i.e. photocurrents). The efficiency of this process relies heavily on the lifetime of the excitons: the higher the efficiency, the longer the exciton lifetime. Therefore, in order to directly compare the exciton lifetime between the two films, we performed TRPL measurements. The TRPL data reveal that the PL lifetime is longer for the HO film (∼6.25 ns) than the RO film (∼1.26 ns), which indicates that carrier lifetime is longer for the HO film (i.e. non-radiative recombination processes have been suppressed in HO film), possibly due to the larger grain size and lower GB density [44]. The origin of the longer PL lifetime in HO film can also be related to the low energy edge state (LES) that is unique to RP perovskites with $n > 2$ [44, 45]. The excitons can be dissociated at the LES that provide a long PL lifetime with suppressed non-radiative recombination. The photo-carriers localized at the LESs were confirmed previously to undergo an ultrafast dissociation to free carriers, which is advantageous for the photodetector application [41]. The existence of LESs can be indirectly detected by PL spectra shown in figure 3(d) and PL lifetime. The lower energy emission peak was shown at ∼760 nm with a full width at half maximum of ∼58.5 nm of HO phase, both of which correspond well to the previously observed PL spectrum due to the emission from the LES for $n = 4$ RP films [44]. On the contrary, the PL peak position of the RO film was at ∼650 nm unlike the emission from the LESs, indicating the lack of LESs within the film. In addition, the PL lifetime of HO film matches well with that of the reported value in literature for LES [41, 44, 45].

To enhance the understanding of the device performance variation between the two devices, we also conducted temperature-dependent device characterizations (figure 4). As seen from the temperature-dependence of the photo- and dark current of RO and HO devices (see figure S9 in the supplementary data), we found that both the photo-and dark current were thermally activated. Therefore, we proceeded with extracting the activation energies for the transport by plotting Arrhenius plot as shown in figures 4(a) and (b). The Arrhenius plot allows us to extract the activation energies for charge and ion-transport in an OHP film by using Nernst–Einstein relation, $\sigma(T) = \left(\frac{\sigma_0}{T}\right)\exp\left(-\frac{E_a}{kT}\right)$, where k is the Boltzmann constant, σ_0 is a constant, and E_a is the ion activation energy [46, 47]. Practically, using the slope of the $\ln(\sigma T)$ versus $-1/kT$ graph, the activation energy can be derived. The calculated activation energies of all cases were attached right beside the fits. From figures 4(a) and (b), it can be seen that the activation energies of the HO phase are generally smaller than those of the RO phase, either with or without light illumination. Since the trap density of GBs is a detrimental factor for charge transport, it is natural that the activation energy values are higher in the RO phase than in the HO phase. Within the low-temperature region where the ion migration is negligible [47], the electronic contribution

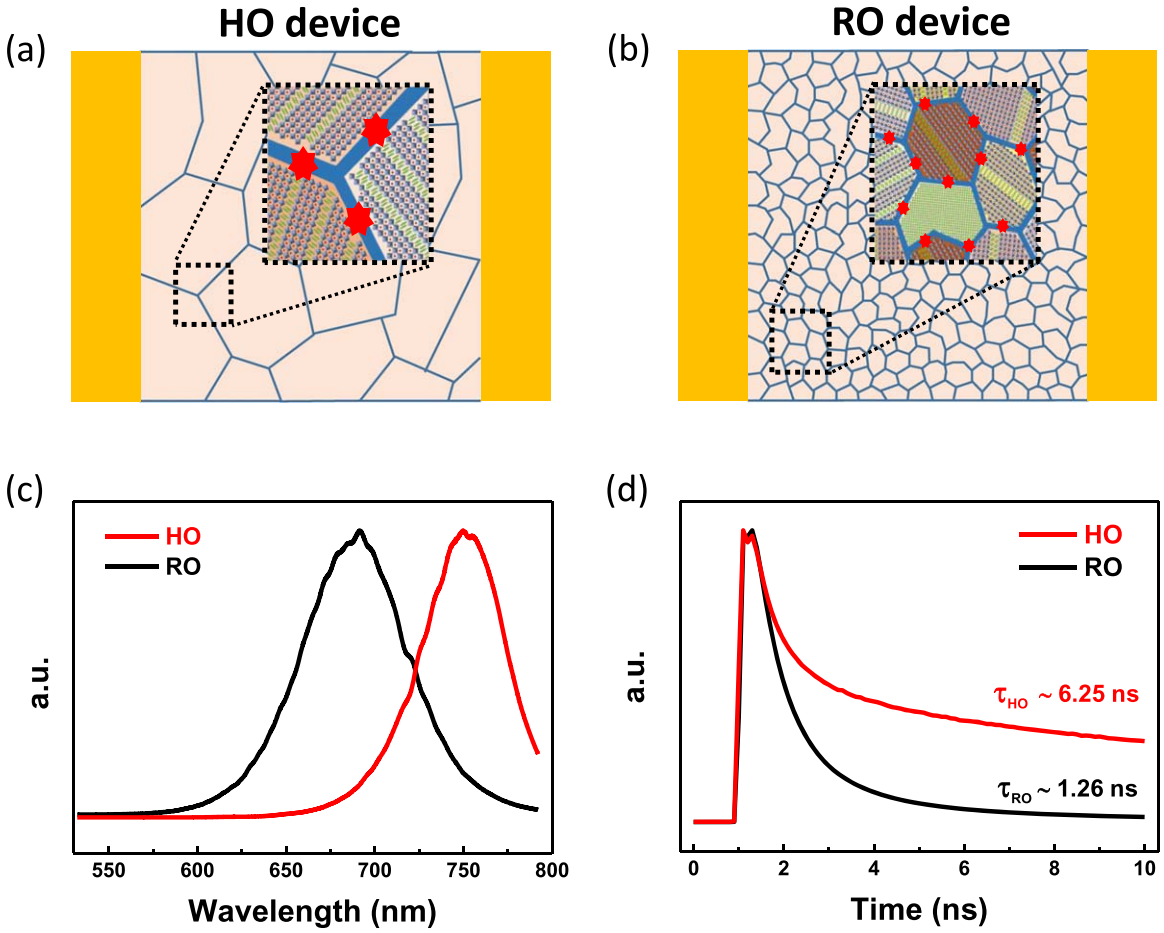

Figure 3. Schematic images of the (a) HO and (b) RO devices. The enlarged images show trap densities in grain boundaries and different lattice orientations. (c) PL spectra of the HO and RO films. (d) TRPL data of the HO and RO films. Derived carrier lifetimes are attached.

can be considered to dominate rather than the ionic contribution. In the dark condition, the activation energy in the low-temperature region turns out to be 25 meV for HO phase, which is lower than the 42 meV for RO phase. Under light illumination, activation energies of the photocurrents are determined to be 18 meV for the HO phase and 59 meV for the RO phase. These activation energy values are comparable to those of previous report that studied $n = 4$ single crystal RP perovskite films; which are 25 meV for the dark condition and 28 meV for the light condition [47]. Traps in GBs of OHPs are shallow rather than deep [48–50]. Yin *et al* revealed that GBs in OHPs do not have deep trap states in the bandgap and generate only shallow point defects [50]. Since the range of thermal energy difference in our experiment is within several tens of meV, only shallow traps are affected during the temperature control. Consequently, the higher density of shallow traps in the RO phase causes the larger current variation according to the temperature. These results support that the lower density of GBs is likely to be the origin of the better device performance in HO device. The mobilities of the light condition at 10 V bias were calculated to be about 3.3 cm^2 V^{-1} s^{-1} for the HO phase and 2.3 cm^2 V^{-1} s^{-1} for the RO phase, which are comparable to previous results using polycrystalline 2D perovskite films [51]. Detailed calculation process is presented in the supplementary data (section 11).

Meanwhile, the transition of the activation energy occurs around 220 K as shown in figures 4(a) and (b). This transition can be caused by ion migration in the high-temperature region, which is mainly due to diffusion of ion vacancies [52, 53]. Unlike 3D counterparts, it is revealed that the ion migration is suppressed in RP perovskites, since the activation energies of ion vacancy migration is large due to the presence of organic spacers which obstruct diffusion of ions [46, 47, 54]. However, our data suggest that the ion migration was not perfectly suppressed since we observed the transition of the activation energy as shown in figure 4(a) for both dark currents of the HO and RO films. The extracted activation energies for the dark currents at the high-temperature region ($T > 220$ K) were found to be 0.23 eV for the RO phase and 0.12 eV for the HO phase. This difference is estimated to be originated from the presence of GBs which are known to act as ion migration paths. Thus, relatively larger activation energies in the high-temperature region than the low-temperature region are likely to be the result of the additional ionic contribution in the current. We assumed the overall conductivity in the high-temperature region can be split to ionic and electronic contributions [55], $\sigma = \sigma_i + \sigma_e = \frac{\sigma_{i0}}{T}\exp(-E_i/kT) + \frac{\sigma_{e0}}{T}\exp(-E_e/kT)$, where σ_i is ionic contribution in the current, σ_e is electronic current contribution, σ_{i0} and σ_{e0} are constants, E_i is the activation energy for the ionic

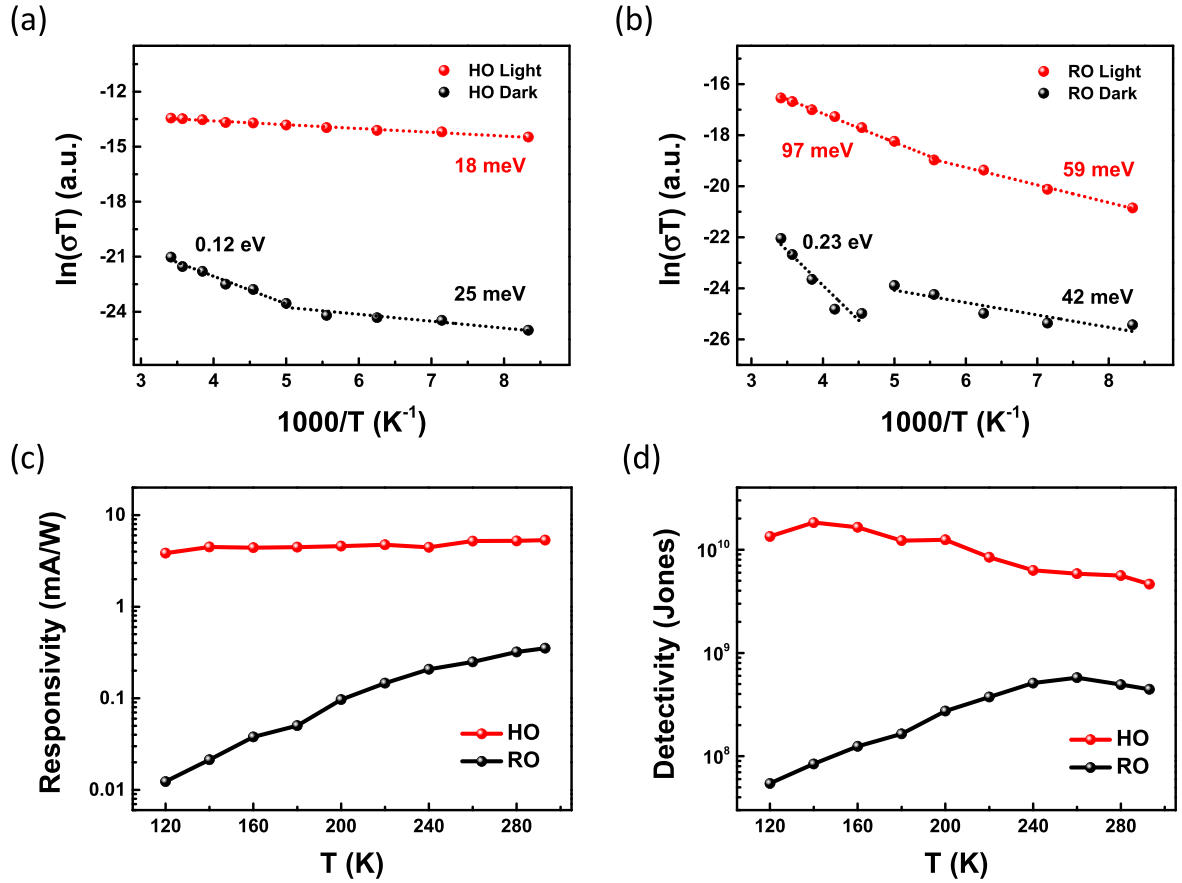

Figure 4. Arrhenius plots for the (a) HO device and (b) RO device. Calculated ion activation energies are attached beside the fitting lines. (c) Temperature-dependent responsivity behavior of the HO and RO devices. (d) Temperature-dependent specific detectivity behavior of the HO and RO devices.

contribution, and E_e is the activation energy for the purely electronic contribution. The E_e can be obtained from the low-temperature region data and was found as 25 meV for the HO phase and 42 meV for the RO phase (figures 4(a) and (b)). From these, we could extract the E_i by double exponential fitting using Nernst–Einstein relation (figure S10 in the supplementary data). Specifically, we utilized $\sigma T \propto \exp(-E_a/kT)$, and compared whether the double or single exponential model fits better by using the Levenberg–Marquardt method. As seen from figure S10, the double exponential model fits better in the HO phase than the single exponential fit (i.e. comparable contributions from electronic and ionic processes) whereas a single exponential model fits better in the RO phase (i.e. a dominant ionic contribution). The corresponding ion activation energies were determined to be 0.40 eV for the HO phase and 0.23 eV for the RO phase (section 12 in the supplementary data). The larger activation energy of the HO phase agrees with our results above that ion migration is more difficult to occur in the HO phase with the less number of ion migration paths provided by GBs.

On the other hand, the transitions of activation energies almost disappear when the light is illuminated, as shown in figures 4(a) and (b). In the HO phase with the lower density of GBs, the transition of the activation energy vanishes (figure 4(a)), which means the ionic contribution becomes insignificant. But, in the RO phase where the density of GBs is high, the transition can be slightly seen (figure 4(b)), which means the ionic contribution is not negligible. However, the transition of the activation energy was greatly weakened; the activation energies for the RO phase were found to be ~97 meV in the high temperature region ($T > 220$ K) and ~59 meV ($T < 220$ K) in the low temperature region (figure 4(b)). We infer that a large number of photo-generated carriers significantly increases the electronic contribution in the current, so that the ionic current contribution becomes negligible. In other words, $\sigma_e \gg \sigma_i$ for both phases over the entire temperature range.

In figures 4(c) and (d), we show the corresponding temperature-dependent device performance parameters, responsivity and detectivity of both phases, respectively. By definition, R is mainly influenced by the photocurrent value. Both the dark and photocurrents of both phases monotonically increase with temperature (see figure S9), as supported by a previous result for the RP perovskite photodetector [45]. The temperature dependence of the responsivity value of RO device was stronger since the photocurrent of the RO device was more thermally activated (figure 4(a)). In terms of the temperature dependence of the detectivity values (figure 4(b)), the detectivity tends to increase as temperature decreases down to around 140 K in HO device. This behavior is originated from the stronger activation energy of the dark current in the HO device compared to that of the photocurrent.

4. Conclusion

In summary, we investigated the photodetector performance according to the crystallinity and orientation of crystals of polycrystalline $BA_2MA_3Pb_4I_{13}$ perovskite film. The structural characteristics were clearly distinguished between the HO and RO phases, by manipulating the solvent evaporation rate. The photodetector performance of the HO phase was significantly better than that of the RO phase with the responsivity by 15 times and detectivity by 10 times higher in HO phase. This result indicates that the lower trap density in GBs and the existence of LES in HO phase are dominant factors in determining the device performance. Through temperature-dependent measurements, we found that the charge transport in the $n = 4$ RP perovskite film is thermally activated. Also, the ionic contribution to the current was identified to be larger in the RO phase than the HO phase from comparison of the activation energies between the two phases. Our crystallinity-dependent transport analysis will contribute to understanding and improving the device performance of 2D RP perovskite optoelectronic device applications.

Acknowledgments

The authors appreciate the financial support of the National Creative Research Laboratory program (Grant No. 2012026372) through the National Research Foundation of Korea (NRF) funded by the Korean Ministry of Science and ICT and the industry-university cooperation program by the Samsung Electronics Co., Ltd. KK appreciates the financial support by Post-doctoral Science Fellowship from POSCO TJ Park Foundation.

Data availability statement

All data that support the findings of this study are included within the article (and any supplementary files).

ORCID iDs

Keehoon Kang https://orcid.org/0000-0003-1230-3626
Takhee Lee https://orcid.org/0000-0001-5988-5219

References

[1] Yang W S, Noh J H, Jeon N J, Kim Y C, Ryu S, Seo J and Seok S I 2015 *Science* **348** 1234
[2] Green M A, Jiang Y, Soufiani A M and Ho-Baillie A 2015 *J. Phys. Chem. Lett.* **6** 4774
[3] Park N-G 2015 *Mater. Today* **18** 65
[4] Niu T *et al* 2019 *Nano Lett.* **19** 7181
[5] Kim M *et al* 2019 *Joule* **3** 2179
[6] Li G *et al* 2016 *Adv. Mater.* **28** 3528
[7] Wang N *et al* 2016 *Nat. Photon.* **10** 699
[8] Sutherland B R and Sargent E H 2016 *Nat. Photon.* **10** 295
[9] Tan Z-K *et al* 2014 *Nat. Nanotechnol.* **9** 687
[10] Zhao X and Tan Z-K 2020 *Nat. Photon.* **14** 215
[11] Zhao X, Ng J D A, Friend R H and Tan Z-K 2018 *ACS Photonics* **5** 3866
[12] Kang K, Ahn H, Song Y, Lee W, Kim J, Kim Y, Yoo D and Lee T 2019 *Adv. Mater.* **31** 1804841
[13] Jung J-H, Kim S H, Park Y, Lee D and Lee J-S 2020 *Adv. Sci.* **7** 2001367
[14] Yu W *et al* 2018 *Nat. Commun.* **9** 5354
[15] Li F, Ma C, Wang H, Hu W, Yu W, Sheikh A D and Wu T 2015 *Nat. Commun.* **6** 8238
[16] Matsushima T, Hwang S, Sandanayaka A S D, Qin C, Terakawa S, Fujihara T, Yahiro M and Adachi C 2016 *Adv. Mater.* **28** 10275
[17] Dou L, Yang Y, You J, Hong Z, Chang W-H, Li G and Yang Y 2014 *Nat. Commun.* **5** 5404
[18] Kim J H, Williams S T, Cho N, Chueh C-C and Jen A K Y 2015 *Adv. Energy Mater.* **5** 1401229
[19] Bi D, Gao P, Scopelliti R, Oveisi E, Luo J, Grätzel M, Hagfeldt A and Nazeeruddin M K 2016 *Adv. Mater.* **28** 2910
[20] Singh A N, Kajal S, Kim J, Jana A, Kim J Y and Kim K S 2020 *Adv. Energy Mater.* **10** 2000768
[21] Yuan Y and Huang J 2016 *Acc. Chem. Res.* **49** 286
[22] Calado P, Telford A M, Bryant D, Li X, Nelson J, O'Regan B C and Barnes P R F 2016 *Nat. Commun.* **7** 13831
[23] Smith I C, Hoke E T, Solis-Ibarra D, McGehee M D and Karunadasa H I 2014 *Angew. Chem., Int. Ed.* **53** 11232
[24] Cao D H, Stoumpos C C, Farha O K, Hupp J T and Kanatzidis M G 2015 *J. Am. Chem. Soc.* **137** 7843
[25] Tsai H *et al* 2016 *Nature* **536** 312
[26] Stoumpos C C, Cao D H, Clark D J, Young J, Rondinelli J M, Jang J I, Hupp J T and Kanatzidis M G 2016 *Chem. Mater.* **28** 2852
[27] Mao L, Ke W, Pedesseau L, Wu Y, Katan C, Even J, Wasielewski M R, Stoumpos C C and Kanatzidis M G 2018 *J. Am. Chem. Soc.* **140** 3775
[28] Soe C M M *et al* 2017 *J. Am. Chem. Soc.* **139** 16297
[29] Chen Y, Sun Y, Peng J, Tang J, Zheng K and Liang Z 2018 *Adv. Mater.* **30** 1703487
[30] Zhou J, Chu Y and Huang J 2016 *ACS Appl. Mater. Interfaces* **8** 25660
[31] Leng K *et al* 2018 *Nat. Mater.* **17** 908
[32] Zhang X *et al* 2017 *Energy Environ. Sci.* **10** 2095
[33] Soe C M M *et al* 2018 *Adv. Energy Mater.* **8** 1700979
[34] Hu Y, Spies L M, Alonso-Álvarez D, Mocherla P, Jones H, Hanisch J, Bein T, Barnes P R F and Docampo P 2018 *J. Mater. Chem.* A **6** 22215
[35] Wang K, Wu C, Yang D, Jiang Y and Priya S 2018 *ACS Nano* **12** 4919
[36] Zhang S *et al* 2019 *Adv. Mater.* **31** 1901090
[37] Blancon J C *et al* 2018 *Nat. Commun.* **9** 2254
[38] Chen A Z, Shiu M, Ma J H, Alpert M R, Zhang D, Foley B J, Smilgies D-M, Lee S-H and Choi J J 2018 *Nat. Commun.* **9** 1336
[39] Chen A Z, Shiu M, Deng X, Mahmoud M, Zhang D, Foley B J, Lee S-H, Giri G and Choi J J 2019 *Chem. Mater.* **31** 1336
[40] Xie C, Mak C, Tao X and Yan F 2017 *Adv. Funct. Mater.* **27** 1603886
[41] Feng J *et al* 2018 *Nat. Electron.* **1** 404
[42] Zhang Y, Tan L, Fu Q, Chen L, Ji T, Hu X and Chen Y 2016 *Chem. Commun.* **52** 5674
[43] Lee H-D *et al* 2019 *Adv. Funct. Mater.* **29** 1901225
[44] Blancon J C *et al* 2017 *Science* **355** 1288
[45] Shi E *et al* 2019 *ACS Nano* **13** 1635
[46] Lin Y, Bai Y, Fang Y, Wang Q, Deng Y and Huang J 2017 *ACS Energy Lett.* **2** 1571

[47] Xiao X, Dai J, Fang Y, Zhao J, Zheng X, Tang S, Rudd P N, Zeng X C and Huang J 2018 *ACS Energy Lett.* **3** 684
[48] Castro-Méndez A-F, Hidalgo J and Correa-Baena J-P 2019 *Adv. Energy Mater.* **9** 1901489
[49] Yin W-J, Shi T and Yan Y 2014 *Appl. Phys. Lett.* **104** 063903
[50] Yin W-J, Shi T and Yan Y 2014 *Adv. Mater.* **26** 4653
[51] Milot R L, Sutton R J, Eperon G E, Haghighirad A A, Martinez Hardigree J, Miranda L, Snaith H J, Johnston M B and Herz L M 2016 *Nano Lett.* **16** 7001
[52] Xing J, Wang Q, Dong Q, Yuan Y, Fang Y and Huang J 2016 *Phys. Chem. Chem. Phys.* **18** 30484
[53] Zheng Y, Niu T, Ran X, Qiu J, Li B, Xia Y, Chen Y and Huang W 2019 *J. Mater. Chem.* A **7** 13860
[54] Lee J-W, Kim S-G, Yang J-M, Yang Y and Park N-G 2019 *APL Mater.* **7** 041111
[55] Lee H, Gaiaschi S, Chapon P, Tondelier D, Bourée J-E, Bonnassieux Y, Derycke V and Geffroy B 2019 *J. Phys. Chem.* C **123** 17728